Additive Manufacturing 45 (2021) 102066

Contents lists available at ScienceDirect

Additive Manufacturing

journal homepage: www.elsevier.com/locate/addma

Crystallographic texture- and grain boundary density-independent improvement of corrosion resistance in austenitic 316L stainless steel fabricated via laser powder bed fusion

Yusuke Tsutsumi [a,b,*,1], Takuya Ishimoto [c,d], Tastuya Oishi [e], Tomoyo Manaka [e], Peng Chen [b], Maki Ashida [b], Kotaro Doi [a], Hideki Katayama [a], Takao Hanawa [b], Takayoshi Nakano [c,d,*]

[a] Research Center for Structural Materials, National Institute for Materials Science (NIMS), 1–2-1 Sengen, Tsukuba, Ibaraki 305-0047, Japan
[b] Institute of Biomaterials and Bioengineering, Tokyo Medical and Dental University (TMDU), 2–3-10 Kanda-Surugadai, Chiyoda, Tokyo 101-0062, Japan
[c] Division of Materials and Manufacturing Science, Graduate School of Engineering, Osaka University, 2–1 Yamadaoka, Suita, Osaka 565-0871, Japan
[d] Anisotropic Design and Additive Manufacturing Research Center, Osaka University, 2–1 Yamadaoka, Suita, Osaka 565-0871, Japan
[e] Graduate School of Medical and Dental Sciences, Tokyo Medical and Dental University, 1–5-45 Yushima, Bunkyo, Tokyo 113-8510, Japan

ARTICLE INFO

Keywords:
Laser powder bed fusion
Austenitic stainless steel
Corrosion resistance
Inclusion
Biomedical applications

ABSTRACT

Improvement of corrosion resistance of austenitic 316L stainless steel via laser powder bed fusion (LPBF) is currently a prominent research topic; however, the effects of crystallographic texture and the related grain boundary density on the corrosion resistance of LPBF-fabricated parts have not been elucidated. For biomedical applications, crystallographic texture control from a single crystalline-like to randomly oriented polycrystalline microstructure is highly attractive for optimizing the mechanical properties (particularly the Young's modulus) of implants. An investigation of the impacts of crystallographic planes and grain boundaries exposed to the biological environment on corrosion behavior is necessary. 316L stainless steels with different crystallographic textures and grain boundary densities were successfully fabricated via LPBF. The corrosion resistances of the LPBF-fabricated specimens were comprehensively assessed by anodic polarization, dissolution, and crevice corrosion repassivation tests. The LPBF-fabricated specimens showed extremely high pitting potentials in the physiological saline compared with the commercially available counterparts, and importantly, excellent pitting corrosion resistance was observed irrespective of the crystallographic planes and grain boundary density exposed. Moreover, the LPBF-fabricated specimens did not show metastable pitting corrosion even in an accelerated test using an acid solution. The repassivation behavior of the specimens was not affected by LPBF. Such a drastic improvement in the corrosion resistances of the LPBF-fabricated specimens might be attributed to suppression of inclusion coarsening owing to the rapid cooling rate during solidification in LPBF. By using LPBF, the desired crystallographic texture can be introduced based on the desired mechanical properties without concern for corrosiveness.

1. Introduction

Corrosion resistance is extremely important for metal components that are used abundantly in various industries such as chemical, petrochemical, marine, and medical. The deterioration reaction of industrial materials sometimes causes serious problems. Hence, it should be controlled for the practical applications of these materials. In the case of metallic biomaterials used in implant devices, the corrosion reaction not only deteriorates the device itself but also adversely affects the living body. In particular, the release of metal ions from the corrosion reaction into a physiological environment is known to cause metal allergy [1–3].

Metallic biomaterials, other than some biodegradable ones, are

* Correspondence to: Corrosion Property Group, Analysis and Evaluation Field, Research Center for Structural Materials, National Institute for Materials Science (NIMS), 1–2-1 Sengen, Tsukuba, Ibaraki 305-0047, Japan.
* Corresponding author at: Division of Materials and Manufacturing Science, Graduate School of Engineering, Osaka University, 2–1 Yamadaoka, Suita, Osaka 565-0871, Japan.
E-mail addresses: TSUTSUMI.Yusuke@nims.go.jp (Y. Tsutsumi), nakano@mat.eng.osaka-u.ac.jp (T. Nakano).
[1] Present address: Research Center for Structural Materials, National Institute for Materials Science (NIMS), 1–2-1 Sengen, Tsukuba, Ibaraki 305–0044, Japan.

https://doi.org/10.1016/j.addma.2021.102066
Received 26 November 2020; Received in revised form 18 May 2021; Accepted 20 May 2021
Available online 27 May 2021

generally selected and/or designed on the bases of corrosion resistance in physiological environments. However, the corrosion of implant devices has not yet been fully controlled. With regard to stainless steel, for example, Tomizawa et al. reported localized corrosion of stainless-steel sternal wires after 22 and 30 years of implantation [4]. Akazawa et al. reported an apparent volume loss in posterior instrumentation rods made of 316L stainless steel [5]. Preventing the corrosion reaction of stainless steel inside a patient's body is highly challenging.

Recently, additive manufacturing (AM) has gained significant attention as an advanced processing technology for the fabrication of metallic products, particularly for applications in the biomedical field. Crystallographic texture control has evolved as a topic of interest in AM research [6–14]. The purpose of utilizing AM is no longer limited to shape control. Metallic materials with strong crystallographic texture exhibit anisotropy in mechanical properties such as the Young's modulus [9,15], yield stress [6,8], and fatigue resistance [15]. To realize implant applications of metallic biomaterials, it is important to reduce their Young's modulus in a specific crystallographic orientation by generating a single crystalline texture via AM fabrication. Furthermore, lowering the Young's modulus of implant biomaterials is important for suppressing stress shielding to bones. 316L stainless steel exhibits the lowest Young's modulus of approximately 94.1 GPa along the $< 100 >$ direction [16], which is lower than the Young's modulus of the Ti-6Al-4 V alloy (110 GPa) frequently used for orthopedic implants. Highly textured 316L with a low Young's modulus would be beneficial for temporary implants [17] such as bone plates and is expected to exhibit a performance equivalent to or superior to that of the Ti-6Al-4 V alloy from the viewpoint of stress-shielding suppression.

For highly textured materials, exposure of certain crystallographic planes to the environment is inevitable. The corrosion resistance of stainless steels prepared by conventional methods depends on their crystallographic planes and grain boundary characteristics [18–21]. The pitting corrosion resistance of austenitic stainless steels, for example, is the highest in the {1 1 1} and {1 0 0} planes with high atomic density, and the lowest in the {110} plane among the low indexed planes [18]. However, although the corrosion resistance of AM-processed 316L stainless steel has been actively researched in recent years [22–28], the crystallographic plane-dependent corrosion resistance of AM-processed stainless steels has not yet been fully revealed. Therefore, the relationship between the crystallographic structure and corrosion behavior of AM-processed materials remains unknown. Corrosion resistance is one of the most important factors that determines the durability, reliability, and safety of newly developed 3D-printed products. In our previous study, we achieved crystallographic texture control with almost no voids via laser powder bed fusion (LPBF), which is a powder bed fusion-type AM process in 316L stainless steel [29].

Therefore, in this study, we investigated the corrosion mechanism of LPBF-processed 316L stainless steel, focusing on its crystallographic planes and grain boundaries. We carried out electrochemical and non-electrochemical corrosion tests to evaluate the localized corrosion resistance and repassivation properties of 316L stainless steel and to determine the amount of metal ions released from it upon immersion in physiological saline.

2. Materials and methods

2.1. Specimen preparation

Gas-atomized 316L stainless steel powder (EOS GmbH, Germany) was used as the primary material for specimen fabrication by LPBF in this study. The nominal composition of the powder was Fe-18Cr-14Ni-2.5Mo-0.03C, and the powder particle size was <53 μm. The LPBF process was performed in an argon atmosphere using a 3D printer (EOSM290, EOS GmbH, Germany).

The crystallographic texture of LPBF-processed materials can be controlled by adjusting the scanning strategy and laser irradiation conditions [9,29]. To examine the evolved texture and planes of interest of the specimens, the *z*-axis was defined as the build direction, and the *x*- and *y*-axes were defined as the laser scanning directions. In this study, we fabricated cubic 316L specimens with dimensions of 11 mm × 11 mm × 11 mm under different LPBF conditions (Table 1). Three types of specimens were fabricated: a specimen with a crystallographic lamellar texture, in which two kinds of grains with {1 1 0} and {1 0 0} orientations along the *x*-axis were alternately stacked (specimen A); a specimen with a single crystalline-like texture with a moderate {1 0 0} pole intensity in the *x*-, *y*-, and *z*-axes (specimen B); and a polycrystalline specimen with relatively random orientation (specimen C) (Fig. 1A and B). The process parameters used for the LPBF fabrication of each specimen are listed in Table 1. These parameters were determined by preliminary examinations in terms of porosity suppression and acquisition of characteristic textures. Crystallographic and grain boundary analyses of the specimens were conducted using an electron backscatter diffractometer (NordlysMax^3, Oxford Instruments, UK) mounted on a field-emission scanning electron microscope (JIB-4610 F, JEOL, Japan). The cross-sections of the specimens were mirror-polished prior to analysis. The crystallographic lamellar texture of specimen A was achieved using the "X-scan strategy," that is, the laser beam was scanned bidirectionally along the *x*-axis without rotation. The other two textures (specimens B and C) were achieved using the "XY-scan strategy," in which the laser was scanned bidirectionally along the *x*- and y-axes alternately with respect to each stacking layer [9]. The formation of a crystallographic texture indicates the presence of grain boundaries in the material. As can be observed from Fig. 1C, specimen C showed the highest grain boundary density, followed by specimens B and A. Table 2 summarizes the microstructural features of the specimens for each cross-section. The *xz*- and *yz*-planes in specimens B and C fabricated using the XY-scan strategy were considered equivalent; therefore, the corrosion tests for the *xz*-plane were omitted. The specimens were cut mechanically to expose their *yz*-, *xz*-, and *xy*-planes. No post-processing was performed on the LPBF specimens.

Generally, stainless steels via common processing show anisotropy in corrosion resistance due to differences in exposed surface. For example, the end faces of stainless steel plates are susceptible to corrosion. This anisotropic corrosion behavior is also known as cut-edge corrosion. This phenomenon is attributed to the different shapes of the inclusions [30,31]. Therefore, two types of commercially available 316L testing coupons were also prepared as reference specimens: a disk-shaped specimen cut from a stainless-steel rod (Nisshin Kogyo, Japan) and a plate-shaped specimen cut from a stainless-steel sheet (Yakin Kawasaki, Japan). These specimens showed different orientations of the testing surface (for evaluating the corrosion resistance) in the cold-working direction. The disk-shaped specimen (8 mm in diameter) was prepared by cutting a stainless-steel rod followed by mechanical grinding along the cutting plane. Meanwhile, the plate-shaped specimen with dimensions of 10 mm × 10 mm was prepared by cutting a large stainless-steel sheet followed by mechanical grinding along the rolling plane. Therefore, in the case of the disk-shaped reference specimen, the surface perpendicular to the cold working direction was exposed for the measurements. Whereas, in the case of the plate-shaped specimen, the surface horizontal to the cold-working direction was exposed. All the testing

Table 1
Parameters used for LPBF fabrication of the specimens.

Specimen	Scanning strategy	Laser power /W	Laser speed /mm/s	Pitch /mm	Layer thickness /mm
Specimen A	X	250	1000	0.08	0.04
Specimen B	XY	350	1100	0.08	0.04
Specimen C	XY	200	1000	0.1	0.04

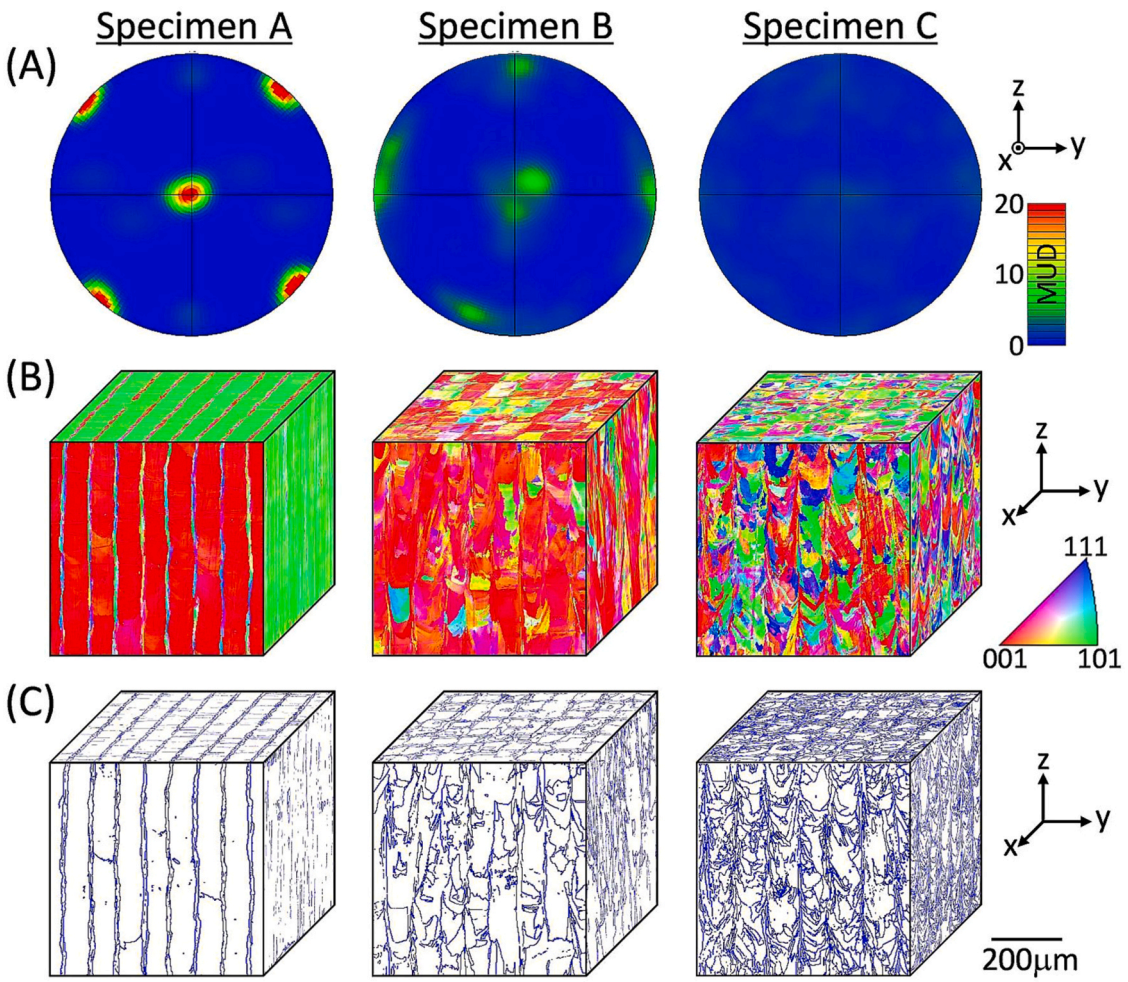

Fig. 1. Crystallographic texture and grain boundary distribution of the laser powder bed fusion (LPBF)-fabricated specimens. (A) {100} pole figures and (B) inverse pole figure maps for the yz-, xz-, and xy-planes, which were perpendicular to the x-, y-, and z-axes, respectively. (C) Maps for the grain boundaries with the misorientation angle of <15°. MUD: multiples of uniform density.

Table 2
LPBF specimen conditions and exposed surface for measurements.

Specimen	Grain boundary density	Specimen plane	Crystal plane exposed preferentially	Measurement
Specimen A	Low	*yz*-plane	Mainly {100}	Performed
		xz-plane	Mainly {110}	Performed
		xy-plane	Mainly {110}	Performed
Specimen B	Middle	*yz*-plane	Moderately {100}	Performed
		xz-plane	Moderately {100}	Not performed
		xy-plane	Moderately {100}	Performed
Specimen C	High	*yz*-plane	Random	Performed
		xz-plane	Random	Not performed
		xy-plane	Random	Performed

surfaces of the specimens were mechanically ground using #150-, #320-, #600-, and #800-grid SiC abrasive papers for exposure to the fresh matrix plane followed by ultrasonication using acetone and isopropanol. Prior to the corrosion tests, the specimens were immersed in ultrapure water for 24 h at room temperature to stabilize the passive layer. The specimens were then kept in an auto-dry desiccator until further use.

2.2. Anodic polarization test

Anodic polarization tests (linear sweep voltammetry) were performed using a potentiostat (HABF-501G, Hokuto Denko, Japan) connected to a function generator (HB-111, Hokuto Denko, Japan) with an analog cable. A saturated calomel electrode (SCE) and platinum electrode were used as the reference and counter electrodes, respectively. The specimens were fixed in a polytetrafluoroethylene holder with an O-ring. The exposed area contacting the electrolyte was 0.35 cm^2 (6.7 mm in diameter). The details of the working electrode are described in our previous study [32]. After immersing the specimens in a standard simulated body fluid (physiological saline: 0.9 mass% NaCl aqueous solution, aerated) at 37 °C, their open circuit potentials (OCPs) were recorded for 10 min. Then, a gradient anodic potential was applied at a constant sweep rate of 1 mVs^{-1} from the initial potential of −50 mV from the OCP. The measurement was stopped when the current density

limit of 1 mAcm^{-2} was recorded. The tests for all five specimens were conducted under open-air conditions and the data are presented as mean ± standard deviation. The difference in the pitting potential was analyzed using one-way analysis of variance followed by Games-Howell multiple comparison test. $P < 0.05$ was considered statistically significant. IBM SPSS Statistics Base 25 software for Windows (SPSS Japan, Japan) was used for the analysis.

2.3. Dissolution test

Dissolution tests were carried out to determine the average corrosion rate and amounts of each metal ion released during the immersion of the specimens in the rapid testing solution. The specimens were first embedded into a cold-mounting epoxy resin and then ground using a #800-grid SiC abrasive paper to expose the intended surface direction. Finally, the specimens were cleaned in ultrapure water using an ultrasonication bath.

The solution used for the dissolution tests comprised a mixture of 5.85 gL^{-1} NaCl and 10.0 gL^{-1} lactic acid. The pH of the solution was 2.30 ± 0.05. This solution was intended to be an accelerated body fluid for rapid testing of the corrosion measurements of dental metallic materials prescribed by the international and Japanese standardization methods (ISO 10271:2011 and JIS T6002: 2014, respectively).

The plastic bottles used as containers for the dissolution test were washed with a 5 vol% nitric acid solution and then rinsed well with ultrapure water. Then, 10 mL of the test solution was placed in a bottle, followed by the addition of the specimens. The bottle was then completely sealed and left at 37 °C for seven days. The metal ion concentrations were measured using an inductively coupled plasma optical emission spectrometer (ICP-OES) (ICPS-7000 ver. 2, Shimadzu, Japan). The amount of ions released from the specimens was calculated by subtracting the values of the blank measurement (the tested solution without a specimen) from their values. The test was performed for three bottles under the same conditions ($N = 3$).

2.4. Crevice corrosion repassivation test

The repassivation behaviors of the specimens recovering from the crevice corrosion state were investigated according to the Japanese industrial standard testing method (JIS G0592: 2002). In this experiment, no specially-designed testing cell was used to induce crevice corrosion, but the area of the crevice that was necessarily formed between the O-ring used and the specimen in the working electrode was utilized, according to Anderson-Wile et al. [33]. The experimental setup for the corrosion repassivation test was the same as that used for the anodic polarization test. After immersing the specimens into a diluted NaCl aqueous solution ([Cl$^-$] = 500 ppm) at 50 °C, potentiodynamic and quasi-galvanostatic polarizations were conducted as follows:

Step 1. Corrosion initiation: Anodic sweep at a constant rate of +30 mVmin^{-1} from the OCP until the critical current of 200 μA.

Step 2. Corrosion growth: Maintained at a constant current of 200 μA for 2 h.

Step 3. Repassivation: Cathodic sweep at a constant rate of −10 mVmin^{-1} from the final potential of the previous step.

The experiment was stopped when the current reached a value of approximately −2 μA, assuring that the crevice corrosion was completely repassivated. The repassivation potential $E_{R,\ crev}$ of the specimens was determined from their potential at zero current. After crevice corrosion repassivation, the surfaces of the specimens were observed to identify the corrosion crevice in the gap area between the O-ring and the specimens. If a corrosion pit was observed on the free surface instead of a crevice, the experimental result was defined as the other parameter, $E_{R,\ pit}$. The test was performed under open-air conditions for all five specimens.

2.5. Analyses of microstructure and inclusion formation

Specimen cross-sections were observed after mirror polishing via optical microscopy (LEXT OLS 4100, Olympus, Japan) and scanning electron microscopy (S-3400N, Hitachi High-Technologies, Japan). To investigate the formation of nanoscale inclusions as well as cellular microstructure in the LPBF-fabricated specimens, transmission electron microscopy (TEM; JEM-3010, JEOL, Japan) was performed. For the TEM observation, thin foils were prepared using a twin-jet electro polishing machine (Tenupol-3, Struers, Denmark) with a solution comprising 90% acetic acid and 10% perchloric acid.

3. Results and discussion

3.1. Anodic polarization test

Fig. 2 shows the polarization curves of the commercially available reference specimens in physiological saline at 37 °C. The disk-shaped specimen exhibited metastable pitting/crevice corrosion under open-circuit conditions just after immersion into the solution. The current density increased with unstable oscillations around the corrosion potential. The breakdown of the passive film occurred at around 0.3 or 0.4 V and the stable pitting corrosion propagated at potentials higher than 0.4 V.

In the case of the plate-shaped specimen, a typical passive material polarization curve was obtained. A passive region was observed until the applied potential reached 0.4 V. The test was repeated five times under the same conditions. Table 3 summarizes the mean and standard deviation of the pitting potentials for the disk- and plate-shaped specimens.

The pitting potential of the plate-shaped specimen was 0.47–0.58 V. The reference specimens exhibited different corrosion behaviors. The disk-shaped specimen was more susceptible to localized corrosion in physiological saline than the plate-shaped one. This can be attributed to the difference in the shapes of the inclusions, which acted as the corrosion initiation sites of these specimens. Generally, the inclusions deform together with the steel matrix during cold working process such as rolling and swaging. In the case of the disk-shaped reference specimen, the exposed surface was perpendicular to the longitudinal (rolling) direction. Thus, the exposed inclusions were deeper and narrower than those of the plate-type specimen. Metastable localized corrosion occurring with deeper inclusions was more resistant to neutralization by convection than that occurring with shallower inclusions. As a result, the localized corrosion in the metastable stage easily propagated to the stable growth stage, which finally caused the lower pitting corrosion potential. Chiba et al. [30,31] reported that the MnS inclusions plays a critical role in the propagation stage of pitting corrosion on stainless

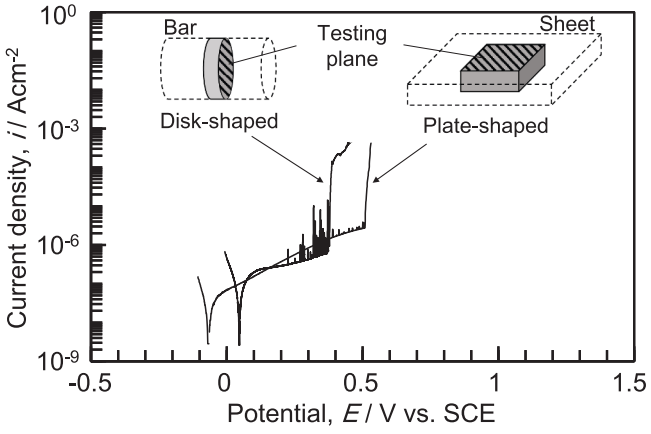

Fig. 2. Polarization curves of disk- and plate-shaped reference specimens prepared from commercially available 316L stainless steel in physiological saline.

Table 3
Summary of the experimental results of anodic polarization tests in physiological saline.

Specimen type	Code	Pitting potential, E_{pit} V vs. SCE	
		Average	Standard deviation
Commercial Rod	Disk- shaped	0.257[a]	0.097
Commercial Sheet	Plate-shaped	0.522[b]	0.039
LPBF-processed Specimen A	*yz*-plane	1.171	0.046
	xz-plane	1.148	0.068
	xy-plane	1.142	0.065
LPBF-processed Specimen B	*yz*-plane	1.067	0.146
	xy-plane	1.156	0.043
LPBF-processed Specimen C	*yz*-plane	1.109	0.047
	xy-plane	1.085	0.039

[a] $P < 0.05$ vs sheet-shaped and all of the LPBF specimens.

[b] $P < 0.05$ vs rod-shaped and all of the LPBF specimens.

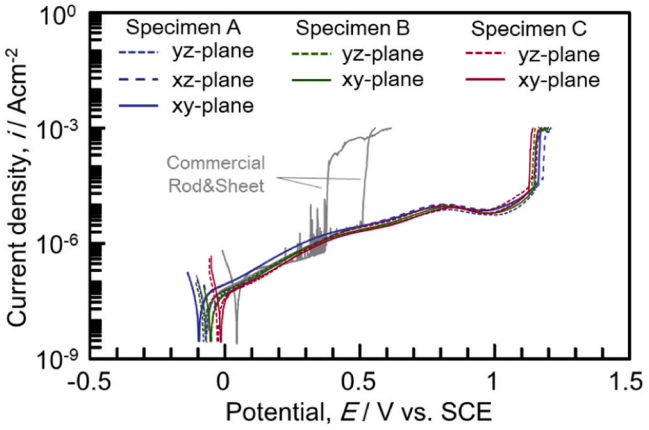

Fig. 3. Polarization curves of the LPBF-fabricated specimens along different exposure planes in physiological saline.

steel.

Fig. 3 shows the polarization curves of LPBF specimens A, B, and C along different exposure planes. As the formation of pores, which are preferential pitting sites [34], was almost completely suppressed in the LPBF specimens, their intrinsic resistivity for pitting corrosion could be analyzed. The polarization curves for the LPBF specimens were different from those of the commercially available reference specimens, as shown in Fig. 2 and Table 3. In the case of the LPBF specimens, the potential range for the passive region expanded without any spikes with an increase in the transient current. Meanwhile, the crystallographic orientations and exposure plane conditions did not affect the polarization curves of the specimens. The pitting potentials of all the LPBF specimens exceeded 1 V, and there was no significant difference in the statistical analysis. The gradual increase in current from 1 V onwards can be attributed to the transpassivation; the complex of iron and chromium oxyhydroxides, a component of the passive film, was electrochemically dissolved under high applied voltage. The anodic current derived from the oxygen evolution reaction may have also overlapped the curve. More specifically, the LPBF specimens did not exhibit pitting corrosion unless their passive films started dissolving under electrochemically accelerated conditions, irrespective of the exposed crystallographic plane and grain boundary density. Moreover, the smooth lines (without any current spike) in the polarization curves of the specimens indicate that there were almost no incubation sites for the initiation of stable/metastable pitting corrosion.

Thus, the corrosion resistance of the specimens was isotropic and independent of the exposed crystallographic plane and grain boundary density, which is beneficial for bone implant applications because any crystallographic orientation can be selected in such cases without the concern of pitting.

3.2. Dissolution test

Fig. 4A shows the dissolution test results of the specimens immersed in an accelerated body fluid for seven days. Among all the specimens, the disk-shaped specimen showed the largest amount of released ions. As shown in Fig. 2, the disk-shaped specimen exhibited temporal pitting and/or crevice corrosion during the initial stage of immersion in a physiological saline solution containing chloride ions. The large number of metal ions detected during the ICP-OES measurement can be attributed to the occurrence of a certain level of the corrosion reaction in the accelerated body fluid with low pH during rapid testing. Fe ions represent a major proportion of the released cations. The Fe, Cr, Ni, and Mo cation fractions (mass%) of the disk-shaped specimen were 67.0%, 20.2%, 11.4%, and 1.4%, respectively. These values are similar to the alloy composition of 316L stainless steel. Therefore, the anode site where the corrosion reaction occurred could be considered as the active dissolution site without the passive film. Fig. 4B shows a magnification of the graph in Fig. 4A. The amounts of the released metal ions were negligibly small and were almost equal to or lower than the detection limit around 0.02 gm^{-2} of the ICP-OES measurement condition in this study. The average amount of Fe released per unit surface area from the specimens except the disk-shaped specimen during the seven-day immersion was 0.0254 ± 0.005 gm^{-2}, which corresponds to a corrosion wastage of 0.170 mm per year. Hence, it can be stated that these specimens maintained their passive state even in the acceleration test environment. The exceptional corrosion resistance of the stainless steel

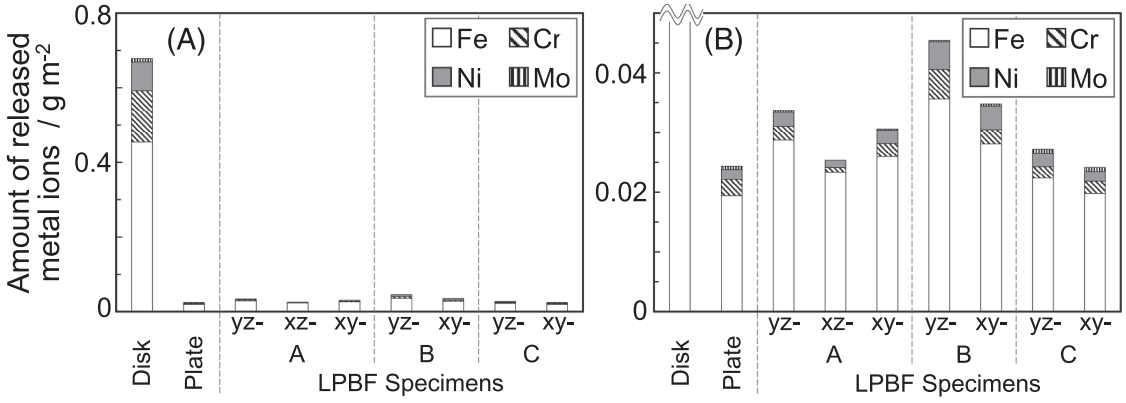

Fig. 4. (A) Result of the dissolution test of immersing the specimens in the accelerated body fluid for rapid testing of corrosion measurements. (B) Magnified graph around the detection level of 0.02 gm^{-2} in this study.

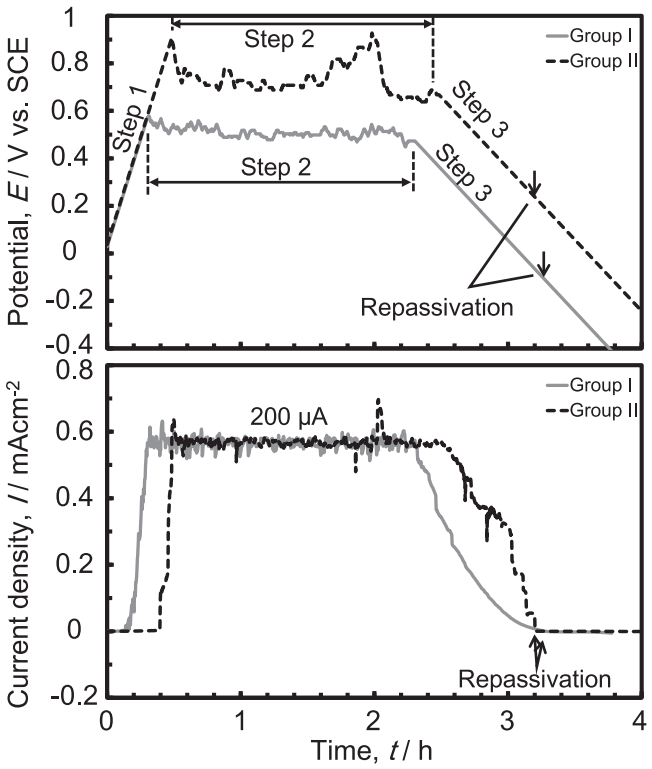

Fig. 5. Changes in potential and current during crevice corrosion repassivation test.

fabricated in this study by LPBF is also bolstered by its isotropic nature (independent of the exposed crystallographic plane and grain boundary density) and the absence of cut-edge corrosion.

3.3. Crevice corrosion repassivation test

Fig. 5 shows the typical results of the crevice corrosion repassivation tests of the specimens in an aqueous solution containing 500-ppm chloride at 50 °C. In the first step for the induction of localized corrosion, the current and potential behaviors of the specimens were similar to those observed in the anodic polarization test. A sharp increase was observed in the current at the critical applied potential because of the breakdown of the passive film. Meanwhile, in the second step for the growth of the localized corrosion, the specimens maintained a current of approximately 200 μA with quasi-galvanostatic control. During the reverse potential scan in the third step, the current decreased and finally became almost zero, indicating complete suppression of the corrosion reaction. The experimental results could be categorized into two groups: lower applied potential in steps 1 and 2, and a gradual current decrease in step 3 (Group I, shown as solid lines in Fig. 5); and higher applied potential in steps 1 and 2 and a rapid current decrease in step 3 (Group II, shown by the broken line in Fig. 5).

Surface observations of the specimens via optical/laser microscopy (LEXT OLS 4100, Olympus, Japan) revealed that the difference in their corrosion behaviors was due to the difference in their localized corrosion types. Fig. 6 shows the optical micrographs and laser micrographic 3D depth profile images of the corrosion sites of the Group I and II specimens, respectively. As can be observed from Fig. 6A, the corroded area exhibited an arc shape with a curvature corresponding to that of the O-ring inserted between the specimen and the electrode holder. Therefore, the corrosion occurring in Group I specimens was confirmed to be crevice corrosion, which propagated along the area beneath the O-ring. Meanwhile, in the case of Group II specimens, corrosion pits were observed at the free surface exposed to the test solution (Fig. 6B). The corrosion pits observed in these specimens were concentric hemispherical. Thus, the corrosion occurring in Group II specimens was found to be pitting corrosion. There was no sign of crevice corrosion in Group II specimens. These results indicate that crevice corrosion occurred on the Group I specimen easily and could be maintained at low applied potentials during the first and second steps of the test; however, they were relatively difficult to repassivate during the third step (Fig. 5). This is because in a crevice environment, the diffusion of matters is limited and neutralization by convection of the solution is difficult to occur. The crevice corrosion repassivation test performed in this study can be used for the diagnosis of corrosion risk in stainless steels. The experimental results of the crevice corrosion-type specimens are more useful as these specimens showed severe corrosion compared with the pitting corrosion-type specimens. The experimental results of the crevice and pitting corrosion repassivation potentials $E_{R,crev}$ and $E_{R,pit}$, respectively, are summarized in Table 4. Each specimen was subjected to five sets of experiments. The experimental results for corrosion pit depths of less than 40 μm were discarded, and the experiment was performed again according to the stipulations of the standard testing method. The average and standard deviation of the E_R values of Group I (crevice corrosion-type, $E_{R,crev}$) and II (pitting corrosion-type, $E_{R,pit}$) specimens were 139.1 ± 33.1 and 309.6 ± 23.7 mV, respectively. The statistical analysis results (Student's *t*-test, $P < 10^{-12}$) showed that crevice corrosion was hard to repassivate compared with pitting corrosion. The specimens showed similar $E_{R,crev}$ values. Moreover, the statistical analysis results of all tested specimen couples were comparable. Thus, the unique metallic structure with strong preferential crystallographic orientation of the LPBF specimens was confirmed to be independent of the repassivation behavior of 316L stainless steel in chloride-containing solutions. More specifically, the crystallographic structure formed by the LPBF process was not the dominant factor for determining the corrosion-free potential range of the specimens.

3.4. Relationship between microstructure and corrosion behavior

The anodic polarization test results (Figs. 2 and 3) reveal that the occurrence of localized corrosion was inhibited in the case of the LPBF specimens. As mentioned earlier, the presence of sulfide-containing inclusions (e.g., MnS and oxides) is partially responsible for the occurrence of localized corrosion on stainless steel. Therefore, in this study, the mirror-finished surfaces of both the commercially available and LPBF-processed specimens (plate-shaped and process condition A, respectively) were observed. The optical and secondary electron micrographs of each specimen are shown in Fig. 7. The commercially available specimens showed a large number of small particles, indicating the presence of exposed inclusions of various sizes. Meanwhile, in the case of the LPBF-processed specimens, the exposed planes (*yz*, *xy*, and *xz*) hardly showed the presence of inclusions. Thus, the precipitation of metal inclusions, which led to localized corrosion, could be effectively inhibited by the LPBF process.

Under the TEM observation, the LPBF-fabricated specimens displayed a cellular microstructure, which is typically observed for LPBF-fabricated metallic products [34], along with nanoscale inclusions (diameter ranging up to 100 nm) distributed extensively, as shown in the bright-field images (Fig. 8). These small inclusions did not deteriorate the localized corrosion resistance of the specimens. The inclusions could not grow because of the extremely high cooling rate during the LPBF process. For austenitic stainless steels, the cooling rate ($\dot{T}$) can be successfully determined from the primary cellular spacing (λ_1) as follows [35,36]:

$$\lambda_1 = 80\dot{T}^{-0.33}$$

As can be observed from Fig. 8, the primary cellular spacing of the specimens was 350–450 nm, resulting in a cooling rate of 6.6×10^6–1.4×10^7 K/s, which is consistent with the values reported

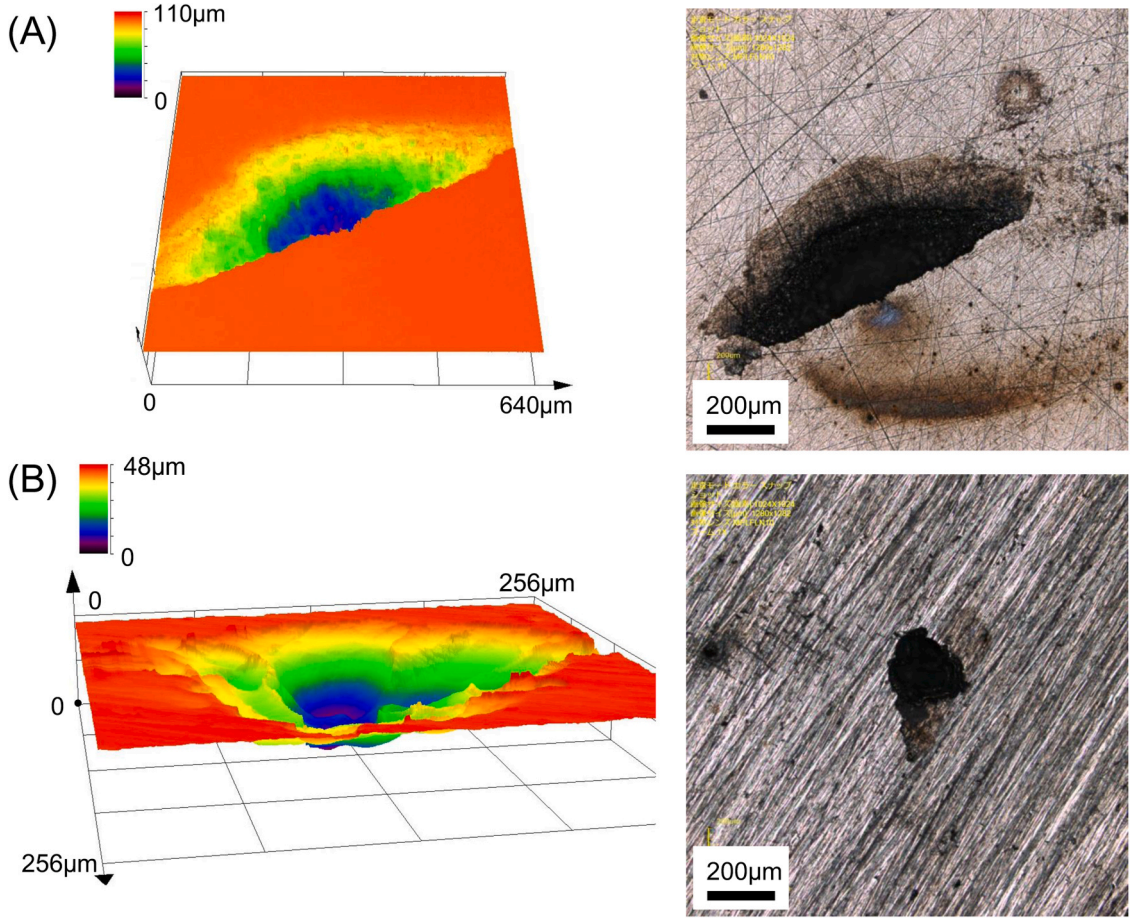

Fig. 6. Typical example of optical micrographs (right) and laser microscopic 3D profiles (left) of (A) crevice corrosion on the Group I specimen and (B) pitting corrosion on the Group II specimen.

Table 4
Summary of the repassivation potential measurements for the reference and LPBF specimens.

Trial	Commercial specimen				LPBF-processed (Specimen A)					
	Disk-shaped		Plate-shaped		*yz*-plane		*xz*-plane		*xy*-plane	
	Group[a]	Potential /mV_{SCE}	Group[a]	Potential /mV_{SCE}	Group[a]	Potential /mV_{SCE}	Group[a]	Potential /mV_{SCE}	Group[a]	Potential /mV_{SCE}
1	I	128.1	II	301.9	I	80.5	II	252.8	I	191.7
2	I	128.3	I	152.1	I	122.4	II	315.7	I	104.3
3	II	323.3	II	334.1	I	147.0	I	110.9	II	332.8
4	I	148.6	II	324.0	II	314.4	I	184.5	II	283.5
5	I	127.4	II	305.5	I	193.0	I	128.8	II	318.6

[a] Group I: Crevice corrosion, Group II: Pitting corrosion.

previously [35,37].

Recently, Chao et al. [38] reported that the pitting potential (E_{pit}) of LPBF-processed 316L stainless steel is 0.74 ± 0.02 V_{SCE}, while that of wrought 316L stainless steel is 0.23 ± 0.03 V_{SCE} in 0.6 M NaCl. Sander et al. [39] reported that 3D-printed 316L stainless steel processed by LPBF showed a nobler E_{pit} value (approximately 300 mV) compared with wrought 316L stainless steel in 0.1 M NaCl. It was hypothesized that LPBF may affect the surface concentration and size distribution of inclusions such that the inclusions are either annihilated or become too miniscule to trigger the formation of pits. The results obtained in this study are consistent with this hypothesis. The E_{pit} values of the LPBF specimens prepared in this study were significantly higher than those reported previously, even under different solution conditions (0.9 mass % nearly equal to 0.15 M NaCl, 37 °C). Considering the fact that the occurrence of metastable pitting was almost entirely eliminated during the anodic scan in the polarization test, the pitting corrosion resistance of the specimens prepared in this study was superior to those of the 316L stainless steel samples reported previously. Sander et al. [39] also reported that LPBF-processed 316L stainless steel with high porosity shows a higher metastable pit frequency and lower repassivation potential than wrought 316L stainless steel. As the LPBF-processed 316L steel fabricated in this study showed almost no metastable pitting corrosion (Fig. 3) and comparable repassivation potential (Table 4) independent of the processing conditions, the fabrication conditions used in this study can be considered as the optimum conditions for the fabrication of LPBF-processed 316L steel with no pores (Fig. 7).

Thus, LPBF can be considered as an innovative and efficient technique for fabricating corrosion-resistant stainless steel. Furthermore, LPBF-processed stainless steel exhibits isotropic corrosion behavior in simulated biological environments despite the formation of a highly

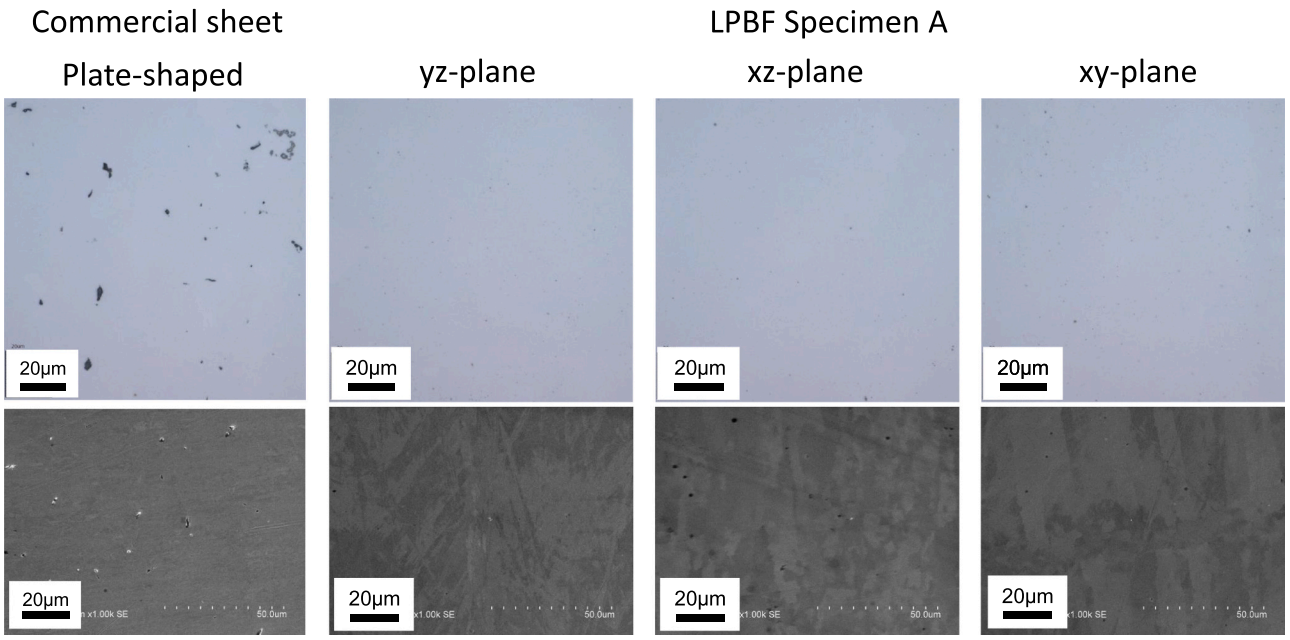

Fig. 7. Surfaces of the mirror-polished 316L stainless steels prepared from commercially available sheet (plate-shaped specimen) and LPBF process (specimen A) observed via laser microscopy (upper) and scanning electron microscopy (lower).

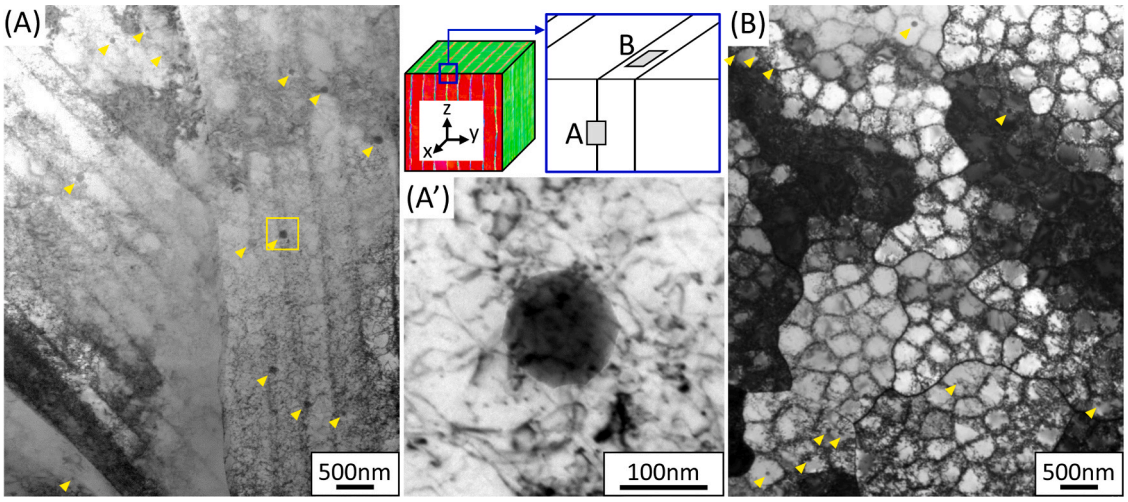

Fig. 8. Transmission electron microscopy images of specimen A: (A) Lateral cross-section and (B) vertical cross-section for the primary cells observed in the yz- and xy-planes, respectively. (A′) Magnified image of an inclusion from the highlighted part in (A). The arrowheads indicate the nanosized inclusions.

textured metallic structure by preferential crystallographic orientation. Importantly, specimens with customized texture can be prepared to achieve the desired mechanical properties without the concern for corrosiveness as long as LPBF is used in manufacturing. LPBF is a promising technique to improve the corrosion resistance of stainless steels by eliminating fatal inclusions, which leads to pitting.

4. Conclusions

In this study, the corrosion resistance of 316L stainless steel fabricated via the LPBF process was investigated. The following conclusions were obtained:

(1) The LPBF fabrication process dramatically improved the localized corrosion resistance of 316L stainless steel under physiological conditions.
(2) The excellent localized corrosion resistance of the LPBF-fabricated specimens was found to be independent of the exposed crystallographic planes and grain boundary densities.
(3) The LPBF process also inhibited the metastable pitting corrosion of the specimens; thus, preventing the deterioration of their repassivation properties.
(4) The excellent corrosion resistance of LPBF-fabricated specimens might be due to the suppression of inclusion growth, which is achieved by a rapid cooling rate estimated as ~10^7 K/s. Only inclusions limited in size to approximately 100 nm or less were present in the LPBF-fabricated specimens.

Funding sources

This work was supported by JSPS KAKENHI Grant Numbers JP17K06835 and JP18H05254. Part of this research is supported by the Research Center for Biomedical Engineering.

CRediT authorship contribution statements

Yusuke Tsutsumi: Writing, Supervision. **Takuya Ishimoto**: Investigation, Writing. **Tatsuya Oishi**: Investigation. **Tomoyo Manaka**: Investigation, Data curation. **Peng Chen**: Validation. **Maki Ashida**: Formal analysis. **Kotaro Doi**: Investigation. **Hideki Katayama**: Resources. **Takao Hanawa**: Supervision. **Takayoshi Nakano**: Project administration, Funding acquisition, Supervision.

Declaration of Competing Interest

The authors declare that they have no known competing financial interests or personal relationships that could have appeared to influence the work reported in this paper.

References

[1] T. Hanawa, Metal ion release from metal implants, Mater. Sci. Eng. C 24 (2004) 745–752, https://doi.org/10.1016/j.msec.2004.08.018.

[2] N. Henrik Nielsen, A. Linneberg, T. Menné, F. Madsen, L. Frølund, A. Dirksen, T. Jørgensen, Allergic contact sensitization in an adult Danish population: two cross-sectional surveys eight years apart (The Copenhagen Allergy Study), Acta Derm. Venereol. 81 (2001) 31–34, https://doi.org/10.1080/000155501750208155.

[3] C. Lidén, S. Carter, Nickel release from coins, Contact Dermat. 44 (2001) 160–165, https://doi.org/10.1034/j.1600-0536.2001.044003160.x.

[4] Y. Tomizawa, T. Hanawa, D. Kuroda, H. Nishida, M. Endo, Corrosion of stainless steel sternal wire after long-term implantation, J. Artif. Organs 9 (2006) 61–66, https://doi.org/10.1007/s10047-005-0321-0.

[5] T. Akazawa, S. Minami, K. Takahashi, T. Kotani, T. Hanawa, H. Moriya, Corrosion of spinal implants retrieved from patients with scoliosis, J. Orthop. Sci. 10 (2005) 200–205, https://doi.org/10.1007/s00776-004-0867-3.

[6] O. Gokcekaya, T. Ishimoto, S. Hibino, J. Yasutomi, T. Narushima, T. Nakano, Unique crystallographic texture formation in Inconel 718 by laser powder bed fusion and its effect on mechanical anisotropy, Acta Mater. 212 (2021), 116876, https://doi.org/10.1016/j.actamat.2021.116876.

[7] T. Ishimoto, K. Hagihara, K. Hisamoto, T. Nakano, Stability of crystallographic texture in laser powder bed fusion: understanding the competition of crystal growth using a single crystalline seed, Addit. Manuf. 43 (2021), 102004, https://doi.org/10.1016/j.addma.2021.102004.

[8] L. Thijs, M.L. Montero Sistiaga, R. Wauthle, Q. Xie, J.P. Kruth, J. Van Humbeeck, Strong morphological and crystallographic texture and resulting yield strength anisotropy in selective laser melted tantalum, Acta Mater. 61 (2013) 4657–4668, https://doi.org/10.1016/j.actamat.2013.04.036.

[9] T. Ishimoto, K. Hagihara, K. Hisamoto, S.H. Sun, T. Nakano, Crystallographic texture control of beta-type Ti–15Mo–5Zr–3Al alloy by selective laser melting for the development of novel implants with a biocompatible low Young's modulus, Scr. Mater. 132 (2017) 34–38, https://doi.org/10.1016/j.scriptamat.2016.12.038.

[10] H.Y. Wan, Z.J. Zhou, C.P. Li, G.F. Chen, G.P. Zhang, Effect of scanning strategy on grain structure and crystallographic texture of Inconel 718 processed by selective laser melting, J. Mater. Sci. Technol. 34 (2018) 1799–1804, https://doi.org/10.1016/j.jmst.2018.02.002.

[11] O. Gokcekaya, N. Hayashi, T. Ishimoto, K. Ueda, T. Narushima, T. Nakano, Crystallographic orientation control of pure chromium via laser powder-bed fusion and improved high temperature oxidation resistance, Addit. Manuf. (2020), 101624, https://doi.org/10.1016/j.addma.2020.101624.

[12] S.H. Sun, K. Hagihara, T. Nakano, Effect of scanning strategy on texture formation in Ni-25at%Mo alloys fabricated by selective laser melting, Mater. Des. 140 (2018) 307–316, https://doi.org/10.1016/j.matdes.2017.11.060.

[13] K. Hagihara, T. Nakano, M. Suzuki, T. Ishimoto, Suyalatu, S.H. Sun, Successful additive manufacturing of $MoSi_2$ including crystallographic texture and shape control, J. Alloy. Compd. 696 (2017) 67–72, https://doi.org/10.1016/j.jallcom.2016.11.191.

[14] X. Wang, J.A. Muñiz-Lerma, O. Sanchez-Mata, M. Attarian Shandiz, N. Brodusch, R. Gauvin, M. Brochu, Characterization of single crystalline austenitic stainless steel thin struts processed by laser powder bed fusion, Scr. Mater. 163 (2019) 51–56, https://doi.org/10.1016/j.scriptamat.2018.12.032.

[15] T.P. Gabb, J. Gayda, R.V. Miner, Orientation and temperature dependence of some mechanical properties of the single-crystal nickel-base superalloy René N4: Part II. Low cycle fatigue behavior, Metal. Trans. A 17 (1986) 497–505, https://doi.org/10.1007/BF02643956.

[16] F. Yang, H. Xue, L. Zhao, X. Fang, H. Zhang, Effects of crystal orientation and grain boundary inclination on stress distribution in bicrystal interface of austenite stainless steel 316L, Adv. Mater. Sci. Eng. 2019 (2019), 2468487, https://doi.org/10.1155/2019/2468487.

[17] A. Parsapour, S.N. Khorasani, M.H. Fathi, Effect of surface treatment and metallic coating on corrosion behavior and biocompatibility of surgical 316L stainless steel implant, J. Mater. Sci. Technol. 28 (2012) 125–131, https://doi.org/10.1016/S1005-0302(12)60032-2.

[18] A. Shahryari, J.A. Szpunar, S. Omanovic, The influence of crystallographic orientation distribution on 316LVM stainless steel pitting behavior, Corros. Sci. 51 (2009) 677–682, https://doi.org/10.1016/j.corsci.2008.12.019.

[19] B.R. Kumar, R. Singh, B. Mahato, P.K. De, N.R. Bandyopadhyay, D.K. Bhattacharya, Effect of texture on corrosion behavior of AISI 304L stainless steel, Mater. Charact. 54 (2005) 141–147, https://doi.org/10.1016/j.matchar.2004.11.004.

[20] D. Lindell, R. Pettersson, Crystallographic effects in corrosion of austenitic stainless steel 316L, Mater. Corros. 66 (2015) 727–732, https://doi.org/10.1002/maco.201408002.

[21] M. Shimada, H. Kokawa, Z.J. Wang, Y.S. Sato, I. Karibe, Optimization of grain boundary character distribution for intergranular corrosion resistant 304 stainless steel by twin-induced grain boundary engineering, Acta Mater. 50 (2002) 2331–2341, https://doi.org/10.1016/S1359-6454(02)00064-2.

[22] M.L.K. Lodhi, K.M. Deen, M.C. Greenlee-Wacker, W. Haider, Additively manufactured 316L stainless steel with improved corrosion resistance and biological response for biomedical applications, Addit. Manuf. 27 (2019) 8–19, https://doi.org/10.1016/j.addma.2019.02.005.

[23] N.S. Al-Mamun, D.K. Mairaj, W. Haider, E. Asselin, I. Shabib, Corrosion behavior and biocompatibility of additively manufactured 316L stainless steel in a physiological environment: the effect of citrate ions, Addit. Manuf. 34 (2020), 101237, https://doi.org/10.1016/j.addma.2020.101237.

[24] S.H. Sun, T. Ishimoto, K. Hagihara, Y. Tsutsumi, T. Hanawa, T. Nakano, Excellent mechanical and corrosion properties of austenitic stainless steel with a unique crystallographic lamellar microstructure via selective laser melting, Scr. Mater. 159 (2019) 89–93, https://doi.org/10.1016/j.scriptamat.2018.09.017.

[25] Q. Chao, V. Cruz, S. Thomas, N. Birbilis, P. Collins, A. Taylor, P.D. Hodgson, D. Fabijanic, On the enhanced corrosion resistance of a selective laser melted austenitic stainless steel, Scr. Mater. 141 (2017) 94–98, https://doi.org/10.1016/j.scriptamat.2017.07.037.

[26] M. Atapour, X. Wang, K. Färnlund, W.I. Odnevall, Y. Hedberg, Corrosion and metal release investigations of selective laser melted 316L stainless steel in a synthetic physiological fluid containing proteins and in diluted hydrochloric acid, Electrochim. Acta 354 (2020), 136748, https://doi.org/10.1016/j.electacta.2020.136748.

[27] D. Kong, C. Dong, X. Ni, L. Zhang, H. Luo, R. Li, C. Man, X. Li, The passivity of selective laser melted 316L stainless steel, Appl. Surf. Sci. 504 (2020), 144495, https://doi.org/10.1016/j.apsusc.2019.144495.

[28] M. Laleh, A.E. Hughes, S. Yang, J. Li, W. Xu, I. Gibson, M.Y. Tan, Two and three-dimensional characterisation of localised corrosion affected by lack-of-fusion pores in 316L stainless steel produced by selective laser melting, Corros. Sci. 165 (2020), 108394, https://doi.org/10.1016/j.corsci.2019.108394.

[29] T. Ishimoto, S. Wu, Y. Ito, S.H. Sun, H. Amano, T. Nakano, Crystallographic orientation control of 316L austenitic stainless steel via selective laser melting, ISIJ Int. 60 (2020) 1758–1764, https://doi.org/10.2355/isijinternational.ISIJINT-2019-744.

[30] A. Chiba, I. Muto, Y. Sugawara, N. Hara, Pit initiation mechanism at MnS inclusions in stainless steel: synergistic effect of elemental sulfür and chloride ions, J. Electrochem. Soc. 160 (2013) C511–C520, https://doi.org/10.1149/2.081310jes.

[31] A. Chiba, I. Muto, Y. Sugawara, N. Hara, Effect of atmospheric aging on dissolution of MnS inclusions and pitting initiation process in type 304 stainless steel, Corros. Sci. 106 (2016) 25–34, https://doi.org/10.1016/j.corsci.2016.01.022.

[32] Y. Tanaka, E. Kobayashi, S. Hiromoto, K. Asami, H. Imai, T. Hanawa, Calcium phosphate formation on titanium by low-voltage electrolytic treatments, J. Mater. Sci. Mater. Med. 18 (2007) 797–806, https://doi.org/10.1007/s10856-006-0004-2.

[33] A.M. Anderson-Wile, B.M. Wile, Q. Wen, H. Shen, Corrosion at the polymer-metal interface in artificial seawater solutions, Int. J. Corros. 2012 (2012) 1–8, https://doi.org/10.1155/2012/496960.

[34] X. Ni, D. Kong, W. Wu, L. Zhang, C. Dong, B. He, L. Lu, K. Wu, D. Zhu, Corrosion behavior of 316L stainless steel fabricated by selective laser melting under different scanning speeds, J. Mater. Eng. Perform. 27 (2018) 3667–3677, https://doi.org/10.1007/s11665-018-3446-z.

[35] M. Ma, Z. Wang, X. Zeng, A comparison on metallurgical behaviors of 316L stainless steel by selective laser melting and laser cladding deposition, Mater. Sci. Eng. A 685 (2017) 265–273, https://doi.org/10.1016/j.msea.2016.12.112.

[36] J.W. Fu, Y.S. Yang, J.J. Guo, W.H. Tong, Effect of cooling rate on solidification microstructures in AISI 304 stainless steel, Mater. Sci. Technol. 24 (2008) 941–944, https://doi.org/10.1179/174328408×295962.

[37] Z. Duan, C. Man, C. Dong, Z. Cui, D. Kong, L. Wang, X. Wang, Pitting behavior of SLM 316L stainless steel exposed to chloride environments with different aggressiveness: pitting mechanism induced by gas pores, Corros. Sci. 167 (2020), 108520, https://doi.org/10.1016/j.corsci.2020.108520.

[38] Q. Chao, V. Cruz, S. Thomas, N. Birbilis, P. Collins, A. Taylor, P.D. Hodgson, D. Fabijanic, On the enhanced corrosion resistance of a selective laser melted austenitic stainless steel, Scr. Mater. 141 (2017) 94–98, https://doi.org/10.1016/j.scriptamat.2017.07.037.

[39] G. Sander, S. Thomas, V. Cruz, M. Jurg, N. Birbilis, X. Gao, M. Brameld, C. R. Hutchinson, On the corrosion and metastable pitting characteristics of 316l stainless steel produced by selective laser melting, J. Electrochem. Soc. 164 (2017) C250–C257, https://doi.org/10.1149/2.0551706jes.